Template Synthesis of Single-Crystal-Like Porous SrTiO₃ Nanocube Assemblies and Their Enhanced Photocatalytic Hydrogen Evolution

Qin Kuang[†,‡] and Shihe Yang[*,†]

[†]Department of Chemistry & William Mong Institute of Nano Science and Technology, The Hong Kong University of Science and Technology, Clear Water Bay, Kowloon, Hong Kong, China

[‡]Department of Chemistry, College of Chemistry and Chemical Engineering, Xiamen University, Xiamen 361005, People's Republic of China

S *Supporting Information*

ABSTRACT: Porous nanostructures of semiconductors are well-known for their ability to enhance the photocatalytic activity thanks to the large specific surface area and abundant active sites for the reactions, interfacial transport, and high utilization of light arising from multireflections in the pores. In this paper, we have successfully fabricated a special porous SrTiO₃ three-dimensional (3D) architecture through a facile hydrothermal reaction at 150 °C, using layered protonated titanate hierarchical spheres (LTHSs) of submicrometer size as a precursor template. The SrTiO₃ architecture is characterized by the 3D assembly of hundreds of highly oriented nanocubes of 60−80 nm by the partial sharing of (100) faces, thereby displaying porous but single-crystal-like features reminiscent of mesocrystals. Our experimental results have shown the key roles played by the template effect akin to that in topotactic transformation in crystallography and Ostwald-ripening-assisted oriented attachment in the formation of such nanocube assemblies. Compared to the solid SrTiO₃ photocatalysts previously synthesized by high-temperature solid-state methods, the as-synthesized porous SrTiO₃ nanocube assemblies have relatively large specific surface areas (up to 20.83 m²·g⁻¹), and thus they have exhibited enhanced photocatalytic activity in hydrogen evolution from

water splitting. Expectantly, our synthetic strategy using LTHSs as the precursor template may be extended to the fabrication of other titanate photocatalysts with similar porous hierarchical structures by taking advantage of the diversity of the perovskite-type titanate.

KEYWORDS: *strontium titanate, template synthesis, porous structure, nanocube assemblies, hydrogen evolution*
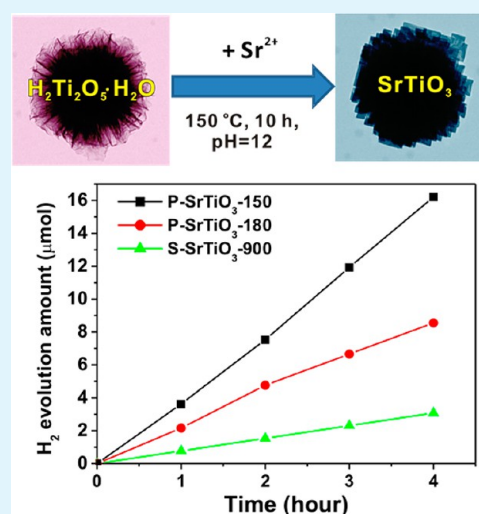
1. INTRODUCTION

In the past decades, semiconductor-based photocatalysis has attracted intensive attention because of its wide applications in the degradation of organic pollutants, hydrogen and oxygen evolution from water splitting, reduction of carbon dioxide, etc.[1−3] Great efforts have been devoted to improving the photocatalytic efficiency of semiconductor photocatalysts, which strongly depends on their morphologies and surface structures. For this reason, semiconductor photocatalysts with various controlled morphologies and exposed facets have been fabricated to acquire high photocatalytic activity.[4−8] Typically, hierarchically porous nanostructures are found to be greatly desirable for photocatalytic semiconductors considering the large specific surface area and abundant active sites for the reactions, interfacial transport, and efficient light trapping and utilization arising from pore-induced multireflections.[5,6,9] Unfortunately, fine control of hierarchically porous structures is still a tremendous challenge because of the limitations of photocatalyst materials in the inherent crystallization habit, although significant progress has been achieved in recent years.

Strontium titanate (SrTiO₃) as an important member of the perovskite-type multimetal oxide family has been regarded as one of the most promising photocatalysts for water splitting and photodegradation of organic pollutants because of its strong catalytic activity, high chemical and photochemical stability, and good biological compatibility.[10−13] Compared to the well-known semiconductor photocatalyst TiO₂, the conduction band and valence band edges of SrTiO₃ are 200 mV more negative, a favorable feature for efficient photoelectrochemical water splitting without an applied bias. Recently, a variety of SrTiO₃ nanoparticles with specific morphologies (e.g., nanocubes, nanorods, nanowires, and nanotubes) have been fabricated via high-temperature solid-state reaction, molten salt methods, hydrothermal or solvothermal methods, sol−gel methods, etc.[14−25] However, to our knowledge, a porous architecture with a three-

Scheme 1. Schematic Synthetic Procedure of Single-Crystal-Like Porous SrTiO$_3$ Nanocube Assemblies
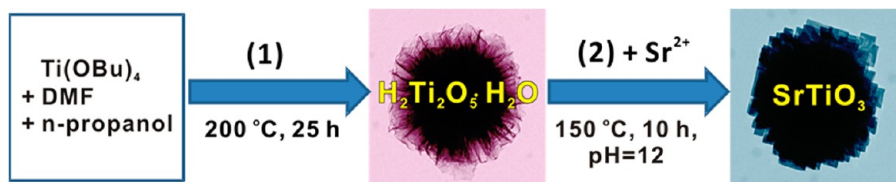
dimensional (3D) hierarchical structure has seldom been reported until now.[17−19] Topochemical reactions using appropriate precursor templates appear to be promising to create porous nanomaterials with 3D hierarchical structures because they can generate abundant pores via crystallographic transformations while roughly maintaining the original morphology of the precursor.[26,27] For SrTiO$_3$, protonated titanate nanofibers have been frequently used as the precursor to obtain one-dimensional porous nanostructures due to structural comparability between protonated titanate and SrTiO$_3$.[21−24] However, so far, this synthetic strategy has not yet been applied to fabricate 3D hierarchical and porous SrTiO$_3$ nanostructures.

In this paper, we have successfully synthesized a special porous SrTiO$_3$ architecture with 3D hierarchical structure via a facile hydrothermal route, using the flower-like layered protonated titanate hierarchical spheres (LTHSs) of submicrometer size as both a precursor and a template. The as-prepared porous SrTiO$_3$ architecture is built by assembling highly oriented nanocubes of 60−80 nm with partially shared (100) faces, converging to a single-crystalline mesocrystal. Our experimental results revealed that a template effect acting on the topochemical-like transformation and Ostwald-ripening-assisted oriented attachment have played key roles in the formation of such nanocube assemblies. In this dynamic assembly process, the appropriate reaction temperature is crucial to balancing the crystallographic transformation to the SrTiO$_3$ nanocubes and the concomitant formation of pores between the nanocube blocks, leading eventually to the successful construction of well-defined, hierarchically architectured assemblies. Furthermore, those porous SrTiO$_3$ nanocube assemblies were demonstrated to exhibit enhanced photocatalytic activity in hydrogen evolution from water splitting because of their porous structure and relatively large specific surface area.

2. EXPERIMENTAL SECTION

2.1. Chemicals. Tetrabutyl titanate [Ti(OBu)$_4$; 97%], *N,N*-dimethylformamide (DMF; HPLC grade), isopropyl alcohol (IPA; 99.7%), strontium chloride hexahydrate (SrCl$_2$·6H$_2$O; 99%), sodium hydroxide (NaOH; 99%), cetyltrimethylammonium bromide (CTAB; 99%), methanol (CH$_3$OH; AR), and chloroplatinic acid hexahydrate [H$_2$PtCl$_6$·(H$_2$O)$_6$; 99.9%] were purchased from Sigma-Aldrich Chemical Reagent Co., Ltd. Strontium carbonate (SrCO$_3$; AR) was supplied by Sinopharm Chemical Reagent Co., Ltd. Degussa P25 was purchased from Shanghai Haiyi Co. All reagents were used directly without any further purification.

2.2. Syntheses of Samples. Single-crystal-like porous SrTiO$_3$ nanocube assemblies were synthesized via a two-step process, as schematically illustrated in Scheme 1. In the first step, the flower-like LTHS precursor was prepared according to the solvothermal process reported by Lou's group with some minor modifications.[28] Typically, Ti(OBu)$_4$ (1 mL) was dropwise added into a mixed organic solvent consisting of DMF (10 mL) and IPA (20 mL) under stirring, and then the resulting solution was transferred to a 50 mL Teflon-lined autoclave. After reaction at 200 °C for 25 h, flower-like LTHSs were

collected by centrifugation, washed thoroughly with ethanol, and dried in a vacuum oven. In the second step, the LTHSs (20 mg) as precursors were ultrasonically dispersed in a NaOH aqueous solution (18 mL, pH = 12), followed by the addition of CTAB (0.2 mmol) and SrCl$_2$·6H$_2$O (2 mmol) under stirring. The resulting dispersion was transferred into a 25 mL Teflon-lined autoclave and then heated at 150 °C (or 180 °C) for 10 h. Finally, the white product was obtained by centrifugation, washed with distilled water and ethanol, and dried at 60 °C in a vacuum oven. For comparison, some solid SrTiO$_3$ spherical particles as a reference were synthesized by the solid-state reaction of SrCO$_3$ and TiO$_2$ at 900 °C for 12 h, followed by calcination at 1100 °C for 24 h in an alumina crucible in air, according to a previous report.[29] For convenience, the porous products obtained at 150 and 180 °C are denoted as P-SrTiO$_3$-150 and P-SrTiO$_3$-180, respectively, and the solid product obtained at 900 °C is denoted as S-SrTiO$_3$-900.

2.3. Characterization of Samples. Morphologies of the products were examined by scanning electron microscopy (SEM; JEOL 6700F) at an accelerating voltage of 5 kV and transmission electron microscopy (TEM; JEOL 2010F) at an accelerating voltage of 200 kV. The compositions of the products were determined by powder X-ray diffraction (XRD; Philips PW-1830) with Cu Kα radiation (λ = 1.5406 Å). The specific surface area of the products was measured by the Brunauer−Emmett−Teller (BET) method using nitrogen adsorption and desorption isotherms on a Micrometrics ASAP 2020 system. The band gap of the as-synthesized SrTiO$_3$ sample was determined by diffuse-reflectance UV/vis absorption spectrometry on a Perkin-Elmer UV/vis spectrophotometer (model Lambda 20) with an integrating sphere attachment, and BaSO$_4$ was used as the reference. A Fourier transform infrared (FTIR) spectrum was recorded on a Bruker VECTOR 22 spectrometer in the frequency range of 4000−400 cm^{-1}.

2.4. Photocatalytic Hydrogen Evolution from Water Splitting. Hydrogen evolution experiments were carried out in a commercial water-splitting measurement system (Labsolar-III, Beijing Perfectlight Technology Co., Ltd.), which consists of a top window Pyrex reaction chamber connected to a closed gas circulation and evacuation system, a light resource (300 W xenon lamp; PLS-SXE-300UV), and a gas chromatograph (Tianmei GC 7400; argon as the carrier gas; 5 Å molecular sieve column) equipped with a thermal conductivity detector. In our study, platinum nanoparticles that were in situ deposited on SrTiO$_3$ samples by photoreduction were selected as a cocatalyst for photocatalytic hydrogen evolution, and methanol was used as a sacrificial reagent. In a typical synthesis of 1 wt % platinum-loaded SrTiO$_3$, the as-prepared SrTiO$_3$ photocatalyst (20 mg) was dispersed in an aqueous solution of methanol (20% v/v, 10 mL) by ultrasonication for 10 min, and then an aqueous H$_2$PtCl$_6$ solution (51.2 μL, 0.02 mol·L^{-1}) was impregnated into the above solution under magnetic stirring. The resulting suspension was illuminated under a 300 W xenon lamp with a UV/vis reflector (with wavelength of 320−780 nm) for 30 min at room temperature. The color of the suspension turned gray, indicating the successful loading of platinum nanoparticles.

The suspension above was transferred into the reaction chamber containing 90 mL of a methanol aqueous solution with the same concentration (20% v/v) under stirring, and then the reaction chamber was sealed with a quartz top window and evacuated several times to remove the air inside. Under irradiation of the 300 W xenon lamp, the gaseous hydrogen evolved was periodically analyzed by online gas chromatography. To avoid evaporation of the solution

during the irradiation reaction, the temperature of the reaction chamber was maintained at 5 °C by cooling water circulation.

3. RESULTS AND DISCUSSION

3.1. Structural Characterization of the Single-Crystal-Like Porous SrTiO₃ Nanocube Assemblies. Figure 1a
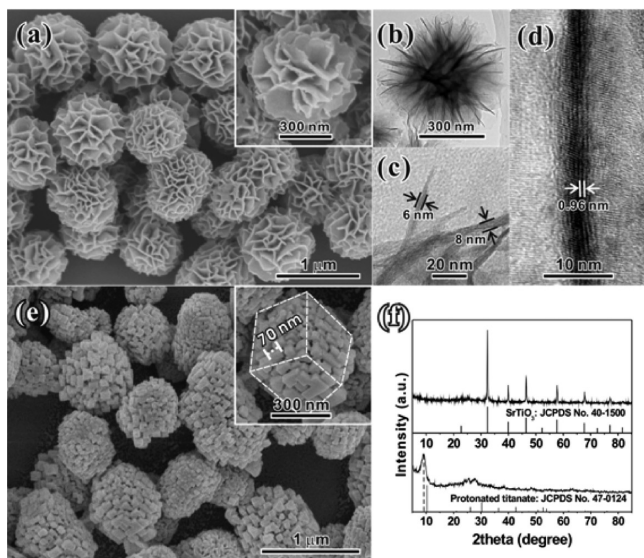

Figure 1. (a) Low-magnification SEM image of the flower-like LTHS precursor. (b) Low-magnification TEM image and (c) partially enlarged image of an individual titanate sphere. (d) HRTEM image taken from one perpendicular nanosheet. (e) Low-magnification SEM image of the sample P-SrTiO₃-150. (f) XRD patterns of the precursor and the sample P-SrTiO₃-150.

shows the typical morphology of the precursor obtained from solvothermal reaction in the first step. It can be seen that the precursor is composed of a large number of flower-like hierarchical spheres of 600−800 nm diameter. The high-magnification SEM image (inset of Figure 1a) and corresponding TEM characterization (Figure 1b) reveal that these flower-like hierarchical spheres are actually built from many interconnected nanosheets. According to the high-magnification TEM image (Figure 1c) recorded from the nanosheet edges, the thicknesses of the nanosheets are in the range of 6−8 nm. In addition, a layered structure is clearly observed in the high-resolution TEM (HRTEM; Figure 1d) image of the nanosheets, in which the interlayer spacing is measured to be about 0.96 nm, corresponding to the (002) plane of protonated titanate. SEM observation (Figure 1e) of the sample P-SrTiO₃-150 indicates that, after hydrothermal treatment with strontium salt at 150 °C, the flower-like hierarchical spheres are transformed into a hierarchically porous architecture of 600−800 nm, which are made of hundreds of cubic primary blocks. A high-magnification SEM image (inset of Figure 1e) shows that these cubic primary blocks are 60−80 nm in size, and they are piled together by the partial sharing of cube faces, leaving pores of 10−20 nm. It is noticed that most of the nanocube assemblies are deformed spheres that look like cuboids when viewed from certain orientations, as shown in the inset of Figure 1e.

The composition of the precursor before and after the hydrothermal treatment was confirmed by XRD. As shown in the bottom curve of Figure 1f, all diffraction peaks of the precursor can be indexed to the lepidocrocite-type protonated

titanate $H_2Ti_2O_5 \cdot H_2O$ (JCPDS no. 47-0124; $a = 18.03$ Å, $b = 3.78$ Å, and $c = 2.99$ Å), which has a layered crystal structure. According to the (200) diffraction peak located at 9.3°, the interlayer spacing of the layered crystal structure is calculated to be about 0.950 nm, which is consistent with the value estimated from the TEM image but slightly larger than the standard value (0.904 nm) of protonated titanate. Previous studies have demonstrated that the intercalation of foreign species (ions or molecules) could induce expansion of the interlayer spacing during formation of the layered titanate.[30] In our case, the intercalated species are probably the decomposed product (such as dimethylamine) of the solvent DMF under hydro-thermal conditions. This is deduced from the fact that the characteristic peaks assigned to N−H can be detected in the IR spectrum of the protonated titanate precursor (Figure S1 in the Supporting Information, SI). For the final product after the hydrothermal treatment, the XRD pattern matches well with the standard one of the perovskite-type SrTiO₃ with a cubic structure (JCPDS no. 40-1500; $a = b = c = 3.936$ Å). No diffraction peaks of residual protonated titanate have been recorded, indicating that the protonated titanate precursor has been completely transformed into SrTiO₃.

The internal structural information of the porous SrTiO₃ nanocube assemblies was obtained by TEM characterization. Figure 2a shows a typical low-magnification TEM image of an individual porous SrTiO₃ nanocube assembly in the sample P-SrTiO₃-150, in which a series of regular, right-angle steps can be clearly observed on the projection outline because of the stacking of primary cubic blocks. Interestingly, the correspond-ing selected area electron diffraction (SAED) pattern (Figure 2b) recorded from the whole assembly only presents a single
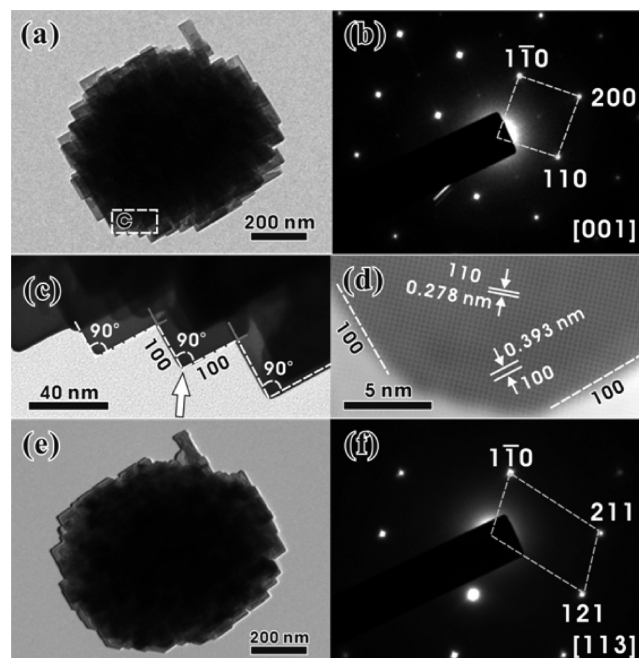
Figure 2. (a) Low-magnification TEM and (b) the corresponding SAED pattern of an individual porous SrTiO₃ nanocube assembly in the sample P-SrTiO₃-150, projected from the [001] zone axis. (c) High-magnification TEM image recorded from zone "c" in part a. (d) HRTEM image taken from a corner of the primary nanocube, as indicated by the arrow in part c. (e) Low-magnification TEM and (f) the corresponding SAED pattern of the individual porous SrTiO₃ nanocube assembly tilted to the [113] zone axis.

set of sharp diffraction spots in a square arrangement, which can be indexed according to the [001] zone axis of the perovskite structure. The high-magnification TEM image (Figure 2c) clearly shows that the primary blocks possess well-defined cubic shape and they are connected with each other by the partial sharing of (100) faces, as indicated by the red crosses. The HRTEM image taken from the corner of a nanocube (Figure 2d) shows a clear two-dimensional lattice with an interlayer spacing of 0.278 nm, corresponding to the (110) planes of $SrTiO_3$, while the interlayer spacing between the planes paralleling the surface of nanocubes is 0.393 nm, corresponding to the (100) planes of $SrTiO_3$. It has been theoretically and experimentally demonstrated that for perovskite the (100) planes have the lowest surface energy, and thus the thermodynamically stable morphology of a particle should be the cube bounded by the (100) facets.[14,15] It should be emphasized that the SAED pattern maintains the single-crystalline feature even when the same nanocube assembly is tilted to another zone axes, e.g., [113] (Figure 2e,f). In addition, we notice that the contour of the porous oriented nanocube assemblies projected in the [001] direction seems close to a rectangle, rather than a disk. This is consistent with the SEM result showing deformed spheres that look like cuboids (the inset of Figure 1e). The overall 3D deformation of the as-synthesized $SrTiO_3$ assemblies from spheres to cuboids implies that the oriented attachment between nanocubes and the subsequent structural rearrangement occur during formation of the porous $SrTiO_3$ nanocube assemblies.

Although no obvious pores are observed by TEM because of overlapping of the primary nanocube blocks, the porous structure of the product was clearly confirmed by nitrogen adsorption−desorption isotherms and Barrett−Joyner−Halenda (BJH) pore-size distribution analysis. As shown in Figure 3,
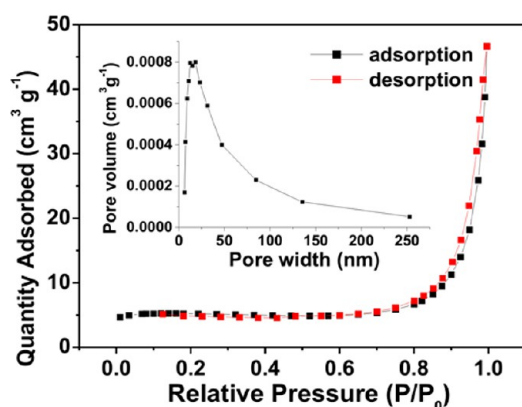
**Figure 3.** Nitrogen adsorption−desorption isotherms and pore-size distribution (inset) of the sample P-SrTiO₃-150.

the sample P-SrTiO₃-150 exhibits an adsorption isotherm that appears to be of an intermediate type between types III and IV.[31,32] The adsorption isotherm at relative pressures of $0 < P/P_0 < 0.8$ indicates low affinity for the nitrogen adsorbate or intrinsically low specific surface area, while at high relative pressures of $0.8 < P/P_0 < 1$, the adsorption isotherm is identified as type IV with hysteresis loop type H3, indicating the presence of mesoporous structures. The BET specific surface area of the as-synthesized $SrTiO_3$ nanocube assemblies is calculated to be 20.83 $m^2 \cdot g^{-1}$, much larger than that (usually below 10 $m^2 \cdot g^{-1}$) of the $SrTiO_3$ particles synthesized by the

solid-state reaction.[29,33] This highlights the advantage of our synthesis method for porous cube assemblies. Furthermore, the BJH pore-size distribution analysis shows that the as-synthesized $SrTiO_3$ nanocube assemblies possess a rather broad pore-size distribution with an average pore radius of 18 nm, in agreement with the value observed from SEM. Overall, the results above have established that the as-synthesized single-crystal-like $SrTiO_3$ product possesses a 3D hierarchical architecture that is porous and assembled from primary nanocubes.

**3.2. Growth Mechanism of the Single-Crystal-Like Porous SrTiO₃ Nanocube Assemblies.** The above structural characterizations have shown that the porous structure of the $SrTiO_3$ nanocube assemblies is built by the partial sharing of faces and piling up of the highly oriented attached primary nanocubes. This feature is different from the porous $SrTiO_3$ spheres synthesized using amorphous TiO_2 gels as precursors, which are composed of randomly oriented spherical particles.[17,18] To probe into the formation mechanism of such a porous $SrTiO_3$ structure built with the 3D assembly of nanocubes, a series of time-dependent synthetic experiments were carried out (Figure 4). At the initial stage of the reaction ($t = 1$ h), the nanosheets of LTHSs begin to roughen, and some cubic rudiments of around 20 nm appear on the outer sheets of the LTHSs (Figure 4a−c). The corresponding SAED pattern (inset of Figure 4b) displays ring diffraction, indicating that these primary cubic nanoparticles are orientationally disordered at this stage. As the reaction proceeds ($t = 3$ h), some well-defined nanocubes of 40−50 nm size are grown on the outer sheets of the LTHSs (Figure 4d−f). A high-magnification TEM image (Figure 4f) shows that the $SrTiO_3$ nanocubes form in adjacent areas with a close orientational relationship, in spite of a certain extent of orientational mismatch. When the reaction continues ($t = 5$ h), the whole spheres from the outer to inner parts have almost completely changed into assemblies of oriented nanocubes and the sizes of the primary nanocubes have increased to around 60 nm (Figure 4g−i). The corresponding SAED pattern (inset of Figure 4h) displays quasi-single-crystalline features, indicating a nearly unanimous orientation of $SrTiO_3$ nanocubes in the whole area. Further XRD characterizations (Figure S2 in the SI) show that the intensity of the diffraction peaks assigned to $SrTiO_3$ increases with the reaction time, indicating that the phase transformation becomes more and more complete.

The influence of the reaction temperature on morphology evolution was also investigated. It is found that the phase transformation is made difficult when the reaction temperature is relatively low, e.g., <120 °C, with the titanate precursor maintaining the original flower-like hierarchical morphology. When the reaction temperature is increased to 180 °C, the porous nanocube assemblies are dominated by those with larger building blocks, as shown in Figure 5a. The size of the building blocks at 180 °C is in the range of 100−200 nm, much larger than that at 150 °C, and some primary cubes have even merged to form nearly solid particles with few pores, as marked with a dashed circle. In addition, some hollow structures assembled with the primary nanocubes are frequently observed in the product (Figure 5b,c). From the corresponding TEM characterization (Figure 5d), it can be seen that these hollow assemblies are also single-crystalline. The high-magnification TEM image (Figure 5e) reveals that there are still some apertures in the hollow zone (i.e., the "e" zone with light contrast), indicating incomplete merging between the nanocube building blocks.
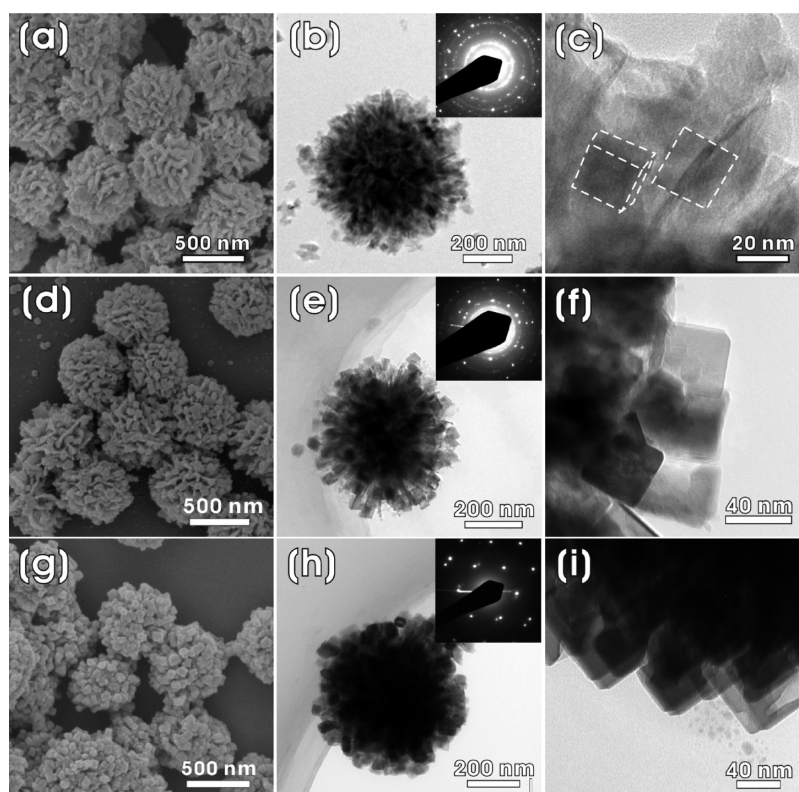
Figure 4. SEM and TEM images of the intermediate products obtained at different reaction times while keeping the reaction temperature at 150 °C: (a–c) 1 h; (d–f) 3 h; (g–i) 5 h.
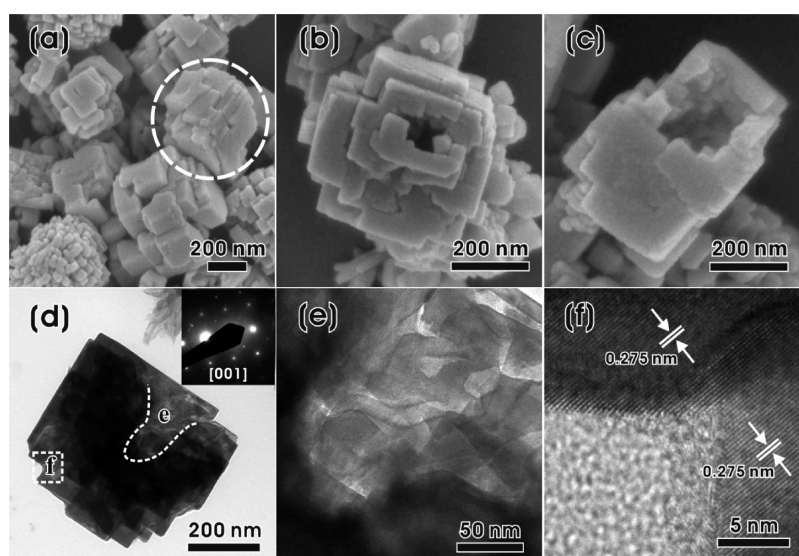

Figure 5. (a–c) SEM images of the nanocube assemblies obtained at 180 °C (i.e., P-SrTiO₃-180) while keeping other conditions constant. (d) TEM and corresponding SAED pattern (inset) of an individual assembly obtained at 180 °C. (e) High-magnification TEM image and (f) HRTEM image recorded from zones "e" and "f" in part d, respectively.

However, the HRTEM image taken from the corner of the assembly (i.e., the "f" zone) shows a continuous (110) lattice, indicating that the boundary between primary blocks has completely disappeared. Therefore, the crystallinity of the porous assemblies prepared at 180 °C is better than that at 150 °C.

On the basis of the above morphological evolution from our experiments, a possible formation mechanism of the single-crystalline porous $SrTiO_3$ architecture built from the nanocube blocks can be proposed. As schematically shown in Figure 6a, the formation process of single-crystalline porous $SrTiO_3$ nanocube assemblies involves two processes, i.e., topotactic transformation in crystallography and self-assembly of nanocubes based on Ostwald-ripening-assisted oriented attachment. Structurally, the perovskite $SrTiO_3$ has some features in common with the protonated titanate. The protonated titanate ($H_2Ti_2O_5 \cdot H_2O$) is a typical layered structure that can be regarded as two-dimensional edge-sharing $[TiO_6]$ octahedral
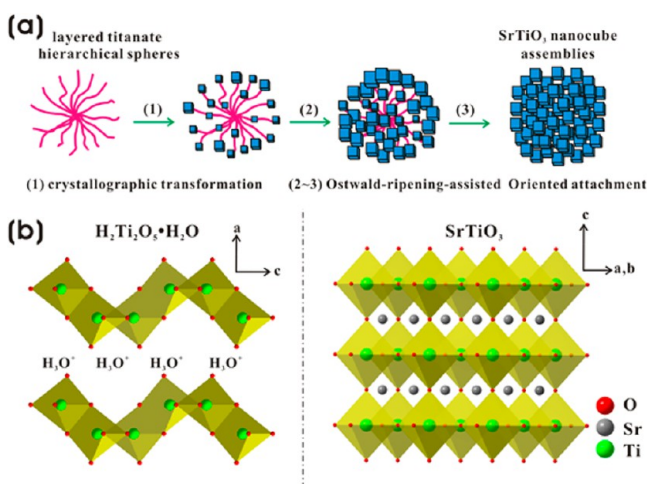
Figure 6. (a) Schematic illustration of the growth mechanism from LTHSs to single-crystalline porous SrTiO$_3$ nanocube assemblies. (b) Crystal structures of layered protonated titanate (left) and perovskite SrTiO$_3$ (right).

sheets separated by H$^+$ ions (Figure 6b, left). Also, the idealized structure of perovskite SrTiO$_3$ can be described as a 3D framework of corner-sharing [TiO$_6$] octahedra with Sr^{2+} ions in the 12-fold cavities between the polyhedra (Figure 6b, right). Because the Sr^{2+} ion radius (0.144 nm) is much smaller than the interlayer spacing (0.95 nm) between the sheets of titanate, Sr^{2+} ions easily enter into the interlayer spaces of the protonated titanate. At the initial stage of the reaction, the hydrothermal treatment initiates local crystallographic transformation of the Sr^{2+}-intercalated titanate, thereby forming small SrTiO$_3$ nanoparticles on the titanate nanosheets. During crystallographic transformation, some vacancies are easily generated between the freshly formed SrTiO$_3$ nanoparticles through a dehydration and condensation process. Considering the fact that the Sr^{2+} ions diffuse into the interlayers of titanate most readily from the outer edge of the nanosheets, it seems rational that crystal transformation from the protonated titanate to cubic SrTiO$_3$ proceeds from the outer to inner parts of hierarchical protonated titanate spheres.

In order to reduce the surface energy, self-assembly of the formed primary SrTiO$_3$ nanocubes subsequently occurs. In this assembly process, the well-known oriented attachment and Ostwald ripening play key roles, which not only enhance the surface recrystallization to form a cubic morphology but also facilitate self-adjustment of the orientations of the primary blocks, resulting in highly oriented piling. The originally formed SrTiO$_3$ nanocubes in the neighborhood tend to keep a close crystallographic orientation because of the template effect of the titanate nanosheet. As the reaction proceeds, the small SrTiO$_3$ nanocubes are unstable and easily dissolved, while the relatively large SrTiO$_3$ nanocubes continue to grow and touch each other because of the Ostwald-ripening mechanism. To reduce the whole surface energy of formed 3D hierarchical structures, the attached SrTiO$_3$ nanocubes rotate themselves to give a coherent lattice structure at the attached interfaces, thereby forming a single-crystal-like hierarchical structure. The conjecture about our proposed Ostwald-ripening-assisted attached attachment mechanism can be forcefully supported by formation of the integrated or hollow assemblies upon increasing reaction temperature, as shown in Figure 5. It is well-known that Ostwald ripening often leads to formation of a

hollow structure[34−36] because the crystallites with relatively small size internally disappear as the reaction proceeds, leaving some vacancies. A high reaction temperature can boost the migration rate of dissolved species and accelerate the growth rate of crystals, thereby facilitating the oriented attachment and Ostwald ripening. For this reason, the integrated or hollow assemblies are easily formed when the reaction temperature increases to 180 °C. From the above analysis, the construction of as-synthesized hierarchical porous nanocube assemblies is actually a dynamic process in which the appropriate reaction temperature is crucial for balancing the crystallographical transformation to the SrTiO$_3$ cubic blocks from the titanate precursor and the formation of pores between the already formed SrTiO$_3$ blocks. A high reaction temperature is conducive to phase transformation, whereas a low reaction temperature is favorable for the formation of pores thanks to slow diffusion of the dissolved species for feeding the growth of the SrTiO$_3$ cubic blocks. In our study, 150 °C appears to be the optimum reaction temperature for the successful construction of well-defined hierarchically porous architecture.

A similar Ostwald-ripening-assisted oriented attachment mechanism has been proposed to explain various single-crystalline hierarchical structures.[19,20,34−36] It should be pointed out that the template effect of the LTHS precursor takes place in the self-assembly of primary nanocubes, which tries to maintain the quasi-spherical architecture of the porous assemblies. Because SrTiO$_3$ primary nanocubes are attached through the partial sharing of (100) faces, the 3D architecture of the finally formed hierarchical structures is prone to deform into a cuboid. On the other hand, the space and tilting between adjacent sheets of the LTHS precursor hinder the merging of adjacent cubic building blocks formed to a certain extent, resulting in the formation of pores in the architecture.

It is worth mentioning that the pH value of the reaction solution was also essential to successful phase transformation from protonated titanate to SrTiO$_3$, which has been demonstrated in previous studies.[22] As shown in Figure S3 in the SI, the precursor LTHSs cannot or can only partially transform into the hierarchical SrTiO$_3$ nanocube assemblies when the basicity of the solution is not strong enough (pH < 12). Viewed from the chemical reaction equation (H$_2$Ti$_2$O$_5$·H$_2$O + 2Sr^{2+} + 4OH$^−$ = 2SrTiO$_3$ + 4H$_2$O), the sufficient alkalinity favors the chemical balance shift toward the right, thereby stimulating the complete transformation from protonated titanate to SrTiO$_3$. However, an excessively alkaline reaction condition is liable to the formation of impurities. As shown in Figure S4 in the SI, some rodlike SrCO$_3$ particles have been produced together with the hierarchical porous SrTiO$_3$ nanocube assemblies when the pH value of the reaction solution is higher than 13.

3.2. Optical Property and Photocatalytic Activity in Hydrogen Evolution from Water Splitting. It is well-known that SrTiO$_3$ is a typical wide-band-gap semiconductor (E_g = 3.25 eV), and it possesses excellent photocatalytic activity under UV light. Herein a diffuse-reflectance UV/vis spectrum was recorded to determine the band gap of the as-synthesized porous SrTiO$_3$ nanocube assemblies. As shown in Figure 7, the SrTiO$_3$ nanocube assemblies only have an absorption band with an absorption edge at 386 nm in the UV region, in agreement with the indirect band-gap transition of 3.25 eV (O 2p → Ti 3d t$_{2g}$/e$_g$).[37]

Considering their potential in solar-energy-harvesting applications, the SrTiO$_3$ nanocube assemblies synthesized at
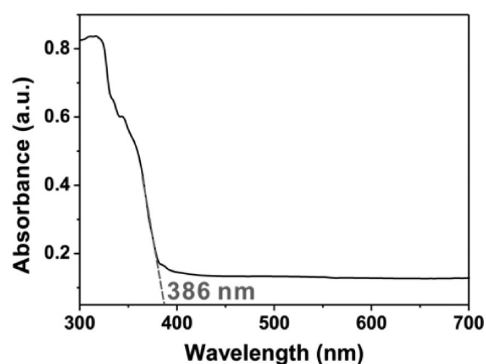
Figure 7. UV/vis absorption spectrum of the as-synthesized porous SrTiO₃ nanocube assemblies obtained at 150 °C (i.e., P-SrTiO₃-150).

150 and 180 °C (i.e., P-SrTiO₃-150 and P-SrTiO₃-180) were subjected to evaluation of their photocatalytic activity in hydrogen evolution from water splitting. In this experiment, the samples were dispersed in an aqueous methanol solution (20% v/v) and then irradiated using a xenon lamp. To confirm the influence of the porous structure on the photocatalytic activity, solid SrTiO₃ particles (i.e., S-SrTiO₃-900), which are 500−700 nm in size and are prepared through a solid-state reaction at 900 °C,[29,38,39] were also measured as a reference (see Figure S5 in the SI for their morphology and structural information). Before measurement, platinum nanoparticles of 1 wt % were in situ deposited on the surface of these SrTiO₃ samples as cocatalysts by the photoreduction method, which is a general method to promote the separation of photogenerated carriers. Figure 8 shows hydrogen evolution curves of the three SrTiO₃
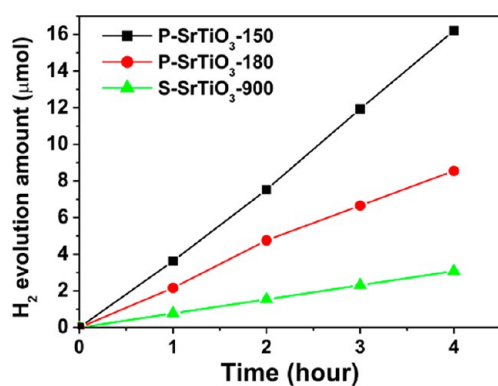
Figure 8. Hydrogen evolution curves of two porous SrTiO₃ nanocube assemblies obtained at 150 and 180 °C (i.e., P-SrTiO₃-150 and P-SrTiO₃-180) and solid SrTiO₃ particles (S-SrTiO₃-900) under irradiation of a 300 W xenon lamp (320 nm < λ < 780 nm).

samples as a function of the irradiation time. For all of the samples, hydrogen can steadily evolve from the methanol aqueous solution under irradiation from a xenon lamp. Within the same irradiation time, the hydrogen-evolved amounts of the

two porous SrTiO₃ nanocube assemblies are much higher than that of the solid SrTiO₃ particles, indicating that the porous structure indeed favors improving the photocatalytic activity of semiconductor photocatalysts. Among the two porous SrTiO₃ samples, P-SrTiO₃-150 synthesized at 150 °C exhibits higher photocatalytic activity because of its comparatively larger surface area. Table 1 summarizes the structural information of the three SrTiO₃ samples and their photocatalytic hydrogen evolution efficiencies. It can be seen that the photocatalytic hydrogen evolution efficiencies of P-SrTiO₃-150 are 1.9 times that of P-SrTiO₃-180 and 5.3 times that of S-SrTiO₃-900. Obviously, the photocatalytic activity of SrTiO₃ photocatalysts is proportional to their specific surface areas. Although one may suspect the role of the sample crystallinity here, we want to call attention to the fact that P-SrTiO₃-180 possesses better crystallinity in direct opposition to its lower photocatalytic activity than P-SrTiO₃-150. This observation clearly indicates that the surface area is the dominating factor here influencing the photocatalytic activity of the photocatalysts.

Finally, we want to point out some potential advantages of our hierarchical porous nanocube assemblies in practical photocatalytic applications compared to isolated nanocrystals. Previous studies have demonstrated that the photocatalytic activity of isolated nanocrystals often decays gradually with time because of the tendency to aggregate into big blobs.[40,41] By contrast, such hierarchical porous architectures as our synthesized 3D nanocube assemblies possess relatively high surface-to-volume ratios, are robust against further aggregation, and therefore should be capable of retaining the relatively high catalytic activities over time for surface reactions. Moreover, the hierarchical porous assemblies are also easier to separate and recycle in practical applications in view of their larger diameters.

4. CONCLUSION

In summary, the template strategy using flower-like protonated titanate nanosheet hierarchical spheres as precursors was proposed to synthesize porous SrTiO₃ hierarchical 3D architectures. Such special hierarchical architectures were constructed with highly oriented nanocubes of 60−80 nm that are assembled by the partial sharing of (100) faces, and thus they possessed massive pores of 10−20 nm. Topographic transformation in crystallography between the layered protonated titanate and perovskite-type structure as well as Ostwald-ripening-assisted oriented attachment was found to a play key role during the formation of such special architectures. As we expected, the as-synthesized porous SrTiO₃ nanocube assemblies obtained at 150 °C exhibited enhanced photocatalytic activity in hydrogen evolution, which is 5.3 times that for the solid SrTiO₃ photocatalysts synthesized by the solid-state reaction because of a relatively large specific surface area (20.83 m²·g⁻¹). It is well-known that perovskite-type titanates are a big family of semiconducting materials with excellent photocatalytic properties. Considering structural comparability

Table 1. Comparison of the Structural Information and Hydrogen Evolution Efficiencies between Two Kinds of Porous SrTiO₃ Nanocube Assemblies and Solid SrTiO₃ Particles Prepared by a Solid-State Reaction

sample	reaction temperature (°C)	particle size (nm)	primary crystallite size (nm)	BET specific surface area (m²·g⁻¹)	hydrogen evolution efficiency (μmol·h⁻¹·g⁻¹)
P-SrTiO₃-150	150	600−800	60−80	20.83	202.6
P-SrTiO₃-180	180	500−700	80−200	7.23	106.8
S-SrTiO₃-900	900	500−700		3.53	38.4

between the layered protonated titanate and perovskite-type structure, our proposed template strategy can be potentially extended for fabricating other perovskite-type titanates with single-crystal-like porous hierarchical structures and enhancing their photocatalytic activity.

■ ASSOCIATED CONTENT

ⓢ Supporting Information

FTIR spectrum of the protonated titanate precursor (Figure S1), XRD patterns of the intermediate products obtained at different reaction times (Figure S2), SEM images of the products obtained at the reaction solutions with pH = 10 and 11 (Figure S3), SEM image and XRD pattern of the product obtained at pH = 13 (Figure S4), and TEM image and XRD pattern of the solid special particles synthesized through a high-temperature solid reaction (Figure S5). This material is available free of charge via the Internet at http://pubs.acs.org.

■ AUTHOR INFORMATION

Corresponding Author
*E-mail: chsyang@utst.hk.

Notes
The authors declare no competing financial interest.

■ ACKNOWLEDGMENTS

■ REFERENCES

(1) Hoffmann, M. R.; Martin, S. T.; Choi, W. Y.; Bahnemann, D. W. *Chem. Rev.* **1995**, *95*, 69.
(2) Kudo, A.; Miseki, Y. *Chem. Soc. Rev.* **2009**, *38*, 253.
(3) Chen, X. B.; Shen, S. H.; Guo, L. J.; Mao, S. S. *Chem. Rev.* **2010**, *110*, 6503.
(4) Han, X. G.; Kuang, Q.; Jin, M. S.; Xie, Z. X.; Zheng, L. S. *J. Am. Chem. Soc.* **2009**, *131*, 3152.
(5) Shchukin, D. G.; Caruso, R. A. *Chem. Mater.* **2004**, *16*, 2287.
(6) Pan, J. H.; Dou, H. Q.; Xiong, Z. G.; Xu, C.; Ma, J. Z.; Zhao, X. S. *J. Mater. Chem.* **2010**, *20*, 4512.
(7) Zhang, L. S.; Wang, W. Z.; Zhou, L.; Xu, H. L. *Small* **2007**, *3*, 1618.
(8) Mclaren, A.; Valdes-Solis, T.; Li, G. Q.; Tsang, S. C. *J. Am. Chem. Soc.* **2009**, *131*, 12540.
(9) Li, Y.; Fu, Z. Y.; Su, B. L. *Adv. Funct. Mater.* **2012**, *22*, 4634.
(10) Townsend, T. K.; Browning, N. D.; Osterloh, F. E. *ACS Nano* **2012**, *6*, 7420.
(11) Ouyang, S. X.; Tong, H.; Umezawa, N.; Cao, J. Y.; Li, P.; Bi, Y. P.; Zhang, Y. J.; Ye, J. H. *J. Am. Chem. Soc.* **2012**, *134*, 1974.
(12) Townsend, T. K.; Browning, N. D.; Osterloh, F. E. *Energy Environ Sci.* **2012**, *5*, 9543.
(13) Hara, S.; Yoshimizu, M.; Tanigawa, S.; Ni, L.; Ohtani, B.; Irie, H. *J. Phys. Chem. C* **2012**, *116*, 17458.
(14) Dang, F.; Mimura, K.; Kato, K.; Imai, H.; Wada, S.; Haneda, H.; Kuwabara, M. *CrystEngComm* **2011**, *13*, 3878.
(15) Nu, J.; Yan, P. X.; Seo, W. S.; Koumoto, K. *J. Nanosci. Nanotechnol.* **2012**, *12*, 2685.
(16) Xie, J.; Ji, T. H.; Ou-Yang, X. H.; Mao, Z. Y.; Shi, H. J. *Solid State Commun.* **2008**, *147*, 226.
(17) Choi, J. Y.; Kim, C. H.; Kim, D. K. *J. Am. Ceram. Soc.* **1998**, *81*, 1353.
(18) Wang, Y. W.; Xu, H.; Wang, X. B.; Zhang, X.; Jia, H. M.; Zhang, L. Z.; Qiu, J. R. *J. Phys. Chem. B* **2006**, *110*, 13835.
(19) Wei, X.; Xu, G.; Ren, Z. H.; Xu, C. X.; Weng, W. J.; Shen, G.; Han, G. R. *J. Am. Ceram. Soc.* **2010**, *93*, 1297.
(20) Zagar, K.; Recnik, A.; Ajayan, P. M.; Ceh, M. *Nanotechnology* **2010**, *21*, 375605.
(21) Li, Y.; Gao, X. P.; Li, G. R.; Pan, G. L.; Yan, T. Y.; Zhu, H. Y. *J. Phys. Chem. C* **2009**, *113*, 4386.
(22) Dong, W. J.; Li, B. J.; Li, Y.; Wang, X. B.; An, L. N.; Li, C. R.; Chen, B. Y.; Wang, G.; Shi, Z. *J. Phys. Chem. C* **2011**, *115*, 3918.
(23) Lee, D. K.; Cho, I. S.; Lee, S.; Kim, D. H.; Shim, H. W.; Kim, D. W.; Hong, K. S. *Eur. J. Inorg. Chem.* **2010**, 1343.
(24) Ma, T. Y.; Li, H.; Ren, T. Z.; Yuan, Z. Y. *RSC Adv.* **2012**, *2*, 2790.
(25) Deng, H.; Qiu, Y. C.; Yang, S. H. *J. Mater. Chem.* **2009**, *19*, 976.
(26) Qiu, Y. C.; Xu, G. L.; Kuang, Q.; Sun, S. G.; Yang, S. H. *Nano Res.* **2012**, *5*, 826.
(27) Qiu, Y. C.; Xu, G. L.; Yan, K. Y.; Sun, H.; Xiao, J. W.; Yang, S. H.; Sun, S. G.; Jin, L. M.; Deng, H. *J. Mater. Chem.* **2011**, *21*, 6346.
(28) Wu, H. B.; Lou, X. W.; Hng, H. H. *Chem.—Eur. J.* **2012**, *18*, 2094.
(29) Wang, D. F.; Ye, J. H.; Kako, T.; Kimura, T. *J. Phys. Chem. B* **2006**, *110*, 15824.
(30) Li, N.; Zhang, L. D.; Chen, Y. Z.; Fang, M.; Zhang, J. X.; Wang, H. M. *Adv. Funct. Mater.* **2012**, *22*, 835.
(31) Garcia-Benjume, M. L.; Espitia-Cabrera, M. I.; Contreras-Garcia, M. E. *Int. J. Photoenergy* **2012**.
(32) Chen, X.; Cheng, J. P.; Shou, Q. L.; Liu, F.; Zhang, X. B. *CrystEngComm* **2012**, *14*, 1271.
(33) Yu, H.; Ouyang, S. X.; Yan, S. C.; Li, Z. S.; Yu, T.; Zou, Z. G. *J. Mater. Chem.* **2011**, *21*, 11347.
(34) Teo, J. J.; Chang, Y.; Zeng, H. C. *Langmuir* **2006**, *22*, 7369.
(35) Chen, X.; Qiao, M.; Xie, S.; Fan, K.; Zhou, W.; He, H. *J. Am. Chem. Soc.* **2007**, *129*, 13305.
(36) Qin, Y.; Zhang, F.; Chen, Y.; Zhou, Y. J.; Li, J.; Zhu, A. W.; Luo, Y. P.; Tian, Y.; Yang, J. H. *J. Phys. Chem. C* **2012**, *116*, 11994.
(37) van Benthem, K.; Elsasser, C.; French, R. H. *J. Appl. Phys.* **2001**, *90*, 6156.
(38) Wang, J. S.; Yin, S.; Komatsu, M.; Sato, T. *J. Eur. Ceram. Soc.* **2005**, *25*, 3207.
(39) Liu, Y.; Xie, L.; Li, Y.; Yang, R.; Qu, J. L.; Li, Y. Q.; Li, X. G. *J. Power Sources* **2008**, *183*, 701.
(40) Zhao, X. W.; Qi, L. M. *Nanotechnology* **2012**, 23.
(41) Li, X.; Duan, Z. Q. *Mater. Lett.* **2012**, *89*, 262.

3690

dx.doi.org/10.1021/am400254n | *ACS Appl. Mater. Interfaces* 2013, 5, 3683–3690